Research article

Michael S.J. Barson, Elmars Krausz, Neil B. Manson and Marcus W. Doherty*

The fine structure of the neutral nitrogen-vacancy center in diamond

https://doi.org/10.1515/nanoph-2019-0142
Received May 14, 2019; revised June 20, 2019; accepted June 23, 2019

Abstract: The nitrogen-vacancy (NV) center in diamond is a widely utilized system due to its useful quantum properties. Almost all research focuses on the negative charge state (NV^-) and comparatively little is understood about the neutral charge state (NV^0). This is surprising as the charge state often fluctuates between NV^0 and NV^- during measurements. There are potentially underutilized technical applications that could take advantage of NV^0, either by improving the performance of NV^0 or utilizing NV^- directly. However, the fine structure of NV^0 has not been observed. Here, we rectify this lack of knowledge by performing magnetic circular dichroism measurements that quantitatively determine the fine structure of NV^0. The observed behavior is accurately described by spin-Hamiltonians in the ground and excited states with the ground state yielding a spin-orbit coupling of $\lambda = 2.24 \pm 0.05$ GHz and a orbital g-factor of 0.0186 ± 0.0005. The reasons why this fine structure has not been previously measured are discussed and strain-broadening is concluded to be the likely reason.

Keywords: nitrogen-vacancy (NV); neutral; diamond; color; center; magnetic circular dichroism (MCD); spectroscopy; spin-orbit; fine structure.

1 Introduction

The nitrogen-vacancy (NV) center is a promising color center in diamond for quantum technology. Applications include nanoscale quantum sensing and quantum information processing. This remarkable utility is due to the useful spin-dependent photodynamics of the center's negative charge state (NV^-). Despite the intense interest in NV^-, surprisingly little is known about the other common charge state of the NV center, the neutrally charged NV^0. It is important to understand NV^0 for a number of reasons. In particular, there is a long standing puzzle as to why the ground state electron paramagnetic resonance (EPR) signal [1] has not been seen in either NV^0 or similar ^2E ground state centers, such as the negatively charged silicon-vacancy [2–4] (SiV^-) and the negatively charged germanium-vacancy [3] (GeV^-) centers.

There are similarities [5, 6] between the Jahn-Teller (JT) induced vibronic structure of the NV^0 ground state and of the poorly understood singlet states of NV^-. The properties of these singlet states and their associated inter-system crossings underpin all of the desirable spin-dependent photodynamics of NV^-, such as spin-polarization and readout. Greater understanding of the NV^- singlet states will lead to the discovery of ways to enhance these properties of NV^- or engineer other defects with improved properties. Due to their similarities, the clues to understanding the behavior of the NV^- singlet levels may lead from a better understanding of the NV^0 ground state.

There are also technical applications using NV^0 in conjuncture with NV^-. One application is controlling the NV charge state to limit the dephasing effect of the electron spin on nearby nuclear spins [7]. A better understanding of the ground state electron spin of NV^0 could also lead to improved control and longer nuclear spin coherence. Another application is the ability to detect the electron ejected to the conduction band during ionization from NV^- to NV^0 for spin-to-charge readout of the NV^- spin [8]. This is used as an alternative spin readout process for quantum applications using NV^-. A further application is using the long-lived photoionization of NV^- to NV^0 for classical data storage [9].

The only previously detected EPR [1] of NV^0 was for the metastable quartet state $^4A_2$. As no ground or excited fine

*Corresponding author: Marcus W. Doherty, Laser Physics Centre, Research School of Physics and Engineering, Australian National University, Acton 2601, Australia, e-mail: marcus.doherty@anu.edu.au. https://orcid.org/0000-0002-5473-6481
Michael S.J. Barson and Neil B. Manson: Laser Physics Centre, Research School of Physics and Engineering, Australian National University, Acton 2601, Australia. https://orcid.org/0000-0003-0247-5619 (M.S.J. Barson), https://orcid.org/0000-0002-5875-4118 (N.B. Manson)
Elmars Krausz: Research School of Chemistry, Australian National University, Acton 2601, Australia. https://orcid.org/0000-0002-8536-6890

structure is determined for NV^0 either by photo-luminescence excitation (PLE) or by EPR, an alternative means of measurement is required. The optical resonance of NV^0 is well known [5]. This provides a starting point and by probing the magneto-optical properties of this resonance, new information regarding the electronic structure of both ground and excited states can be obtained. One such magneto-optical measurement is magnetic circular dichroism (MCD) spectroscopy. MCD is a differential optical spectroscopic technique that determines the difference of left and right circularly polarized light in the presence of an axial magnetic field [10, 11]. This provides quantitative measurements of the magnetic behavior of optical transitions. In particular, the fine structure of the ground and excited states can be extracted from the MCD measurements.

In this paper, we determine the fine structure of NV^0 and develop a simple electronic model that fully describes the observed behavior. The MCD experiment is introduced and it is shown how the electronic model relates the resulting spectra. The results and model allow for the fine structure parameters of the system to be determined. We then discuss why such fine structure behavior has not been observed in previous measurements.

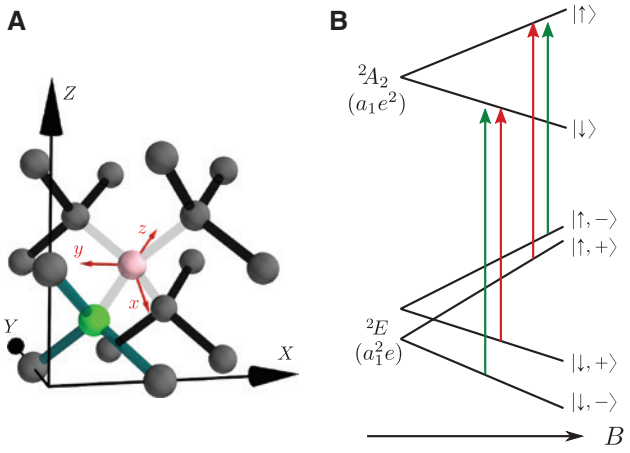

Figure 1: The atomic and electronic description of the NV^0 center. (A) Unit cell of diamond containing a nitrogen vacancy (NV) center with crystallographic coordinates $(X, Y, Z) = ([100], [010], [100])$ and NV coordinates chosen as $(x, y, z) = ([11\bar{2}], [\bar{1}10], [111])$. The carbon atoms are depicted as gray, the nitrogen atom as green, and the vacancy site as pink. (B) Energy levels of the NV^0 ground ^2E (a_1e^2) and excited $^2A_2$ (a_1^2e) states, where the brackets signify the molecular orbitals [14]. The orbital states are denoted by +, − and spin states by ↑, ↓. Left and right circularly polarized optical transitions are denoted by the red and green arrows. The gradients of the ground state resonances with respect to magnetic field are unequal due to the orbital Zeeman competing with spin Zeeman effects.

2 Theory

The NV center consists of a substitutional nitrogen impurity and an adjacent vacancy. The defect in its neutral charge state has five electrons, three from the dangling carbon bonds and two from the dangling nitrogen bond. The negatively charged state gains an additional electron from nearby charge donors (usually nitrogen) [12, 13]. The NV axis (line between nitrogen and vacancy sites) is aligned along a ⟨111⟩ direction and the defect has three-fold rotational symmetry (C_{3v}), as shown in Figure 1A.

The electronic structure of NV^0 consists of a ^2E ground state, $^2A_2$ optical excited level, and an intermediate metastable $^4A_2$ level. The zero phonon line (ZPL) of the $^2E \leftrightarrow {}^2A_2$ occurs at 2.16 eV (575 nm). The $^2A_2$ has no orbital degeneracy and exhibits no zero field fine structure. The ground state ^2E has orbital degeneracy that gives rise to spin-orbit fine structure as shown in Figure 1B. The ^2E fine structure can be described by the Hamiltonian

$$H = g\mu_B \vec{S}\cdot\vec{B} + l\mu_B L_z B_z + 2\lambda L_z S_z, \tag{1}$$

where μ_B is the Bohr magneton, $g \sim 2$ is the spin g-factor and l is the orbital g-factor, λ is the spin-orbit interaction parameter, the orbital $L_i = \sigma_i$ and spin $S_i = \frac{1}{2}\sigma_i$ operators are defined respectively in terms of the Pauli matrices σ_i and z is along the NV axis (see definition of coordinate system in Figure 1A). Note that the effect of strain is not included in the Hamiltonian as measurements using MCD are insensitive to strain, see the Supplementary information for a proof of this. In the presence of a large magnetic field, it is convenient to transform the spin coordinate system so that S_z is parallel to the applied field (i.e. $S_z \to S_z \cos\theta + S_x \sin\theta$), whilst the orbital operators remain unchanged because the orbitals remain defined by the crystal axes. The transformed Hamiltonian is then

$$\begin{aligned} H = {} & \mu_B g S_z B + \mu_B l L_z B\cos\theta \\ & + 2\lambda L_z (S_z\cos\theta + S_x \sin\theta), \end{aligned} \tag{2}$$

For our measurements, the diamond sample had a <100> face that was aligned parallel to the magnetic field, and thus $\cos\theta = \hat{z}\cdot\hat{Z} = 1/\sqrt{3}$. For this field orientation, all possible NV orientations have an equivalent magnetic field projection. The eigenenergies of the transformed Hamiltonian are thus

$$\begin{aligned} E_{\pm\downarrow} &= \pm\mu_B lB\cos\theta - \frac{1}{2}\sqrt{4\lambda^2 + (g\mu_B B)^2 \pm 4\lambda g\mu_B B\cos\theta} \\ E_{\pm\uparrow} &= \pm\mu_B lB\cos\theta + \frac{1}{2}\sqrt{4\lambda^2 + (g\mu_B B)^2 \pm 4\lambda g\mu_B B\cos\theta}, \end{aligned} \tag{3}$$

where the ↑, ↓ signifies spin-up-down states and the ± signifies orbital states with well-defined positive and

negative units of orbital angular momentum about the NV axis. The optical selection rules are such that the ± orbital states participate in R/L circularly polarized transitions, respectively. Care was taken to transform the circularly polarized light from the lab coordinate system into the NV coordinate system, see Supplementary information.

We use MCD to determine the magnetic splitting of the ^2E state. This allows for the spin-orbit parameter λ and orbital g-factor l to be determined. As these measurements are performed at low temperature and high magnetic fields ($k_BT \sim g\mu_B B$), the thermal populations of the ^2E ground state sub-levels must also be included into the model. The optical transition being measured is spin allowed and the energy levels of the excited $^2A_2$ must also be considered. We have assumed a simple spin-1/2 system with a g-factor of 2. Thus the excited state eigenenergies are simply $E_{A\uparrow\downarrow} = E_{ZPL} \pm g\mu_B B/2$, where E_{ZPL} is the optical ZPL energy.

3 Materials and methods

The experimental apparatus is described in Ref. [15]. White light is passed through a double monochromator so as to provide monochromatic light that can be swept in frequency. This light is then passed through a chopper wheel to modulate the intensity (488 Hz modulation frequency). Next the light is filtered to remove second-order diffracted light and is then linearly polarized and passed through a photoelastic modulator which is driven at 50 kHz to create alternatively left and right circularly polarized light. The combination of the chopper wheel and periodic circularly polarized light allows for a heterodyne-based detection process so as to measure small differences in left and right circularly polarized absorption. In this work, the differential absorption is about 10^2 times weaker than the total absorption. The sample is placed in a temperature controlled (1.46–300 K) liquid helium immersion cryostat with a 0–6 T superconducting magnet.

The sample was a CVD grown (Element six) crystal with ~ppm concentration of nitrogen that was irradiated with electrons at a fluence of $10^{17}/cm^2$ and energy of ~2 MeV and then annealed at 750°C for 2 h to create NV centers. The NV^0 ZPL is on top of the NV^- absorption phonon sideband, however, only the difference in absorption ZPL relative to the background is considered. As such, the results are not affected by the presence of the NV^- ZPL. The absorption of NV^0 is weak with about a 7% reduction in transmittance at the peak of the ZPL.

4 Results

The total absorption (Z_{L+R}) and the differential absorption (Z_{L-R}), as shown in Figure 2 are simultaneously acquired. The differential signal $Z_{L-R} = Z_L - Z_R$, is the difference of two nondegenerate absorptive lineshapes and the total absorption $Z_{L+R} = (Z_L + Z_R)/2$ is the arithmetic mean of the two absorptive lineshapes. By comparing the two spectra using either parametric curve fitting or moment analysis [11, 16] the separation and magnitude of the two circularly polarized absorptions can be determined. Moment or curve fitting analyses each have separate benefits and drawbacks and both methods of analysis were pursued in parallel. For curve-fitting, Gaussian lineshapes were used with the free parameters A_1, A_2, σ, μ and d. A_1 and A_2 are the amplitudes of the lines, $2d$ is the separation of the two lines and μ and σ are the shared central position and width of the two lines.

$$Z_{L\pm R}(E) = \frac{A_1}{\sqrt{2\pi\sigma}} e^{\frac{(E-\mu-d)^2}{2\sigma^2}} \pm \frac{A_2}{\sqrt{2\pi\sigma}} e^{\frac{(E-\mu+d)^2}{2\sigma^2}} \quad (4)$$

The moment analysis is performed as described in Ref. [10].

The first MCD quantity we consider describes the probability of absorbing a left or right circularly polarized photon. This can be expressed by the ratio of the zeroth Z_{L+R} and Z_{L-R} spectral moments or the amplitudes (A_1 and A_2) obtained from the parametric curve fitting

$$\frac{\langle Z_{L-R}\rangle_0}{\langle Z_{L+R}\rangle_0} = 2\frac{(P_{-\downarrow} + P_{-\uparrow}) - (P_{+\downarrow} + P_{+\uparrow})}{P_{-\downarrow} + P_{-\uparrow} + P_{+\downarrow} + P_{+\uparrow}} = \frac{A_1 - A_2}{A_1 + A_2}. \quad (5)$$

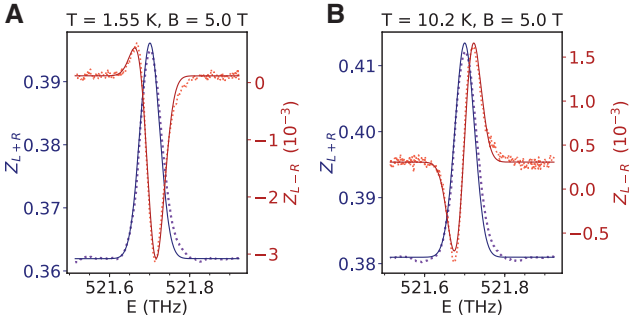

Figure 2: Examples of MCD spectra.
The total (Z_{L+R}) and differential (Z_{L-R}) absorption spectra at B = 5 T and T = 1.55 K (A) and at B = 5 T and T = 10.2 K (B). Notice the change in sign of the Z_{L-R} signal for the higher temperature data. Plots are in units of absorbance $A = \log_{10}\frac{\Phi_i}{\Phi_t}$, where $\Phi_{i,t}$ are the incident and transmitted radiant fluxes. The fits are of the same form as shown in (4).

In the above, the angle brackets $\langle Z_{L+R}\rangle_n$ represent the nth spectral moment. The second MCD quantity is probability weighted transition energies of absorbing a left or right circularly polarized photon. As such, it also provides information regarding the energy separation of the left and right circularly polarized transitions. This quantity can be determined from the ratio of the first and zeroth moments of the Z_{L-R} and Z_{L+R} spectra respectively. This quantity can also be determined by curve fitting using the energy separation ($2d$) and amplitudes (A_1 and A_2) of two lineshapes.

$$\begin{aligned}\frac{\langle Z_{L-R}\rangle_1}{\langle Z_{L+R}\rangle_0} &= [(P_{-\downarrow}(E_{-\downarrow}-E_{A\downarrow})+P_{-\uparrow}(E_{-\uparrow}-E_{A\uparrow}))\\ &\quad -(P_{+\downarrow}(E_{+\downarrow}-E_{A\downarrow})+P_{+\uparrow}(E_{+\uparrow}-E_{A\uparrow}))]\\ &\quad \times\frac{2}{P_{-\downarrow}+P_{-\uparrow}+P_{+\downarrow}+P_{+\uparrow}}\\ &= \frac{4dA_1A_2}{(A_1+A_2)^2}. \end{aligned} \tag{6}$$

In the above, the probabilities P_i are determined from the thermal occupations $P_i = e^{-E_i/k_BT}/\sum_j e^{-E_j/k_BT}$ of the fine structure states of the ^2E level.

The results for a variety of temperatures and magnetic fields are shown in Figure 3. The change in sign of the zeroth and first-order moments for increasing temperature is due to the thermal populations of the ground state sub-levels changing, flipping the likelihood of absorbing a left or right circularly polarized photon.

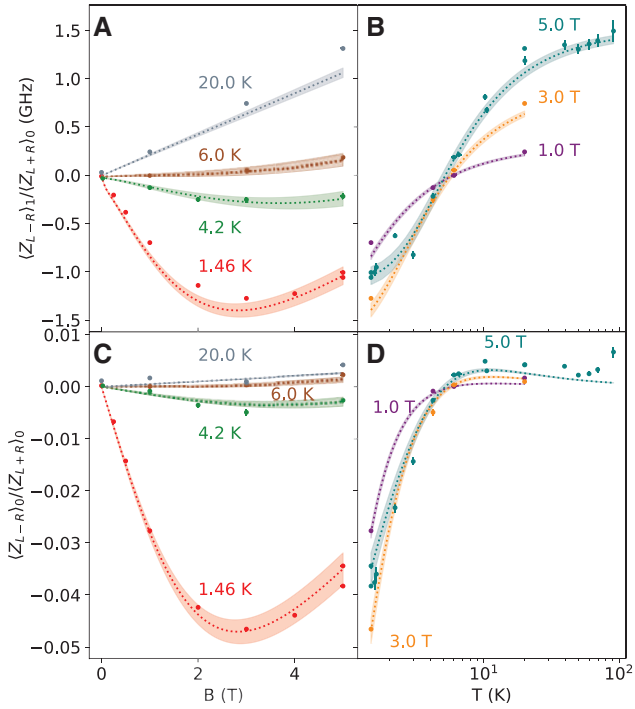

Figure 3: Summary of the MCD results.
The MCD values from (6) for varying magnetic field (A) and temperature (B). MCD values from (5) for varying magnetic field (C) and temperature (D). The points represent the values from curve fitting, the moment analysis points are removed for clarity. The dashed curve is the Hamiltonian model using the average parameter values, $\lambda = 2.24 \pm 0.05$ GHz and $l = 0.0186 \pm 0.0005$, the shaded regions represent the 1σ uncertainty in the average parameter values.

5 Analysis

The data are fitted against the Hamiltonian (2) [via (5) and (6)] using only two free parameters, the spin-orbit coupling λ and the orbital g-factor l, the other parameters $g = 2$ and $\theta = \cos^{-1}(1/\sqrt{3})$ were kept fixed. This fit obtains the values $\lambda = 2.24 \pm 0.05$ GHz and $l = 0.0186 \pm 0.0005$. Due to the difference in methods, the error analysis for both the curve fitting and the moment analysis was performed via a Monte-Carlo method. The raw spectra was modulated with random normally distributed noise with an amplitude equal to the standard deviation of the signal to the sides of the main feature. This was chosen as it represents the noise in the photocurrent signal for a particular spectra. The entire fitting procedure was re-run multiple times to obtain a distribution of the extracted parameters with an associated standard error and mean.

These results show that the orbital g-factor l is reduced by an order of magnitude from the NV$^-$ ^3E level, of which there are three published values (0.10(1) [17], 0.22 [18], and 0.164(6) [19]). There is only one published value of the orbital g-factor for the NV^0 ^2E state of 0.017(2) [19]. This is in reasonable agreement with our value of $l = 0.0186(5)$. The spin-orbit parameter λ is also reduced from its corresponding value in the NV$^-$ ^3E level ($\lambda = 5.3$ GHz [20, 21]). However, the reduction is not as large as for the orbital g-factor (a factor of ~1/2 rather than ~1/10).

6 Discussion

There are a number of possible explanations for the differing reductions of the orbital g-factor and spin-orbit parameter from NV$^-$ to NV^0. Both parameters are affected by the same Ham reduction factor [22, 23] arising from the JT interactions of the NV^0 ^2E or NV$^-$ ^3E levels. If the JT interaction of NV^0 is larger than of NV$^-$ (as indicated by features observed in piezospectroscopy of NV^0 [5]), then this would explain the reduced size of these parameters

in NV^0. However, this explanation would imply that both parameters should be reduced by the same factor.

An alternate or complimentary explanation can be found in how the parameters depend on the defect's molecular orbital structure and local electrostatic potentials. The orbital *g*-factor is proportional to the reduced matrix element $\langle e(\vec{r};\vec{R})||l_z||e(\vec{r};\vec{R})\rangle$, whereas the spin-orbit parameter is $\propto\langle e(\vec{r};\vec{R})||[\vec{\nabla}V_{Ne}(\vec{r}_i,\vec{R})\times\vec{p}]_z||e(\vec{r};\vec{R})\rangle$, where l_z is the orbital angular momentum operator along the axis of the NV center, $[\vec{\nabla}V_{Ne}(\vec{r}_i,\vec{R})\times\vec{p}]_z$ is similarly the axial component of the orbital operator of the spin-orbit interaction, V_{Ne} is the electrostatic interaction between the defect electrons and the nuclei, $\vec{r}$ are the electron coordinates, $\vec{R}$ are the nuclear coordinates, and $e(\vec{r};\vec{R})$ are *e* molecular orbitals in the Born-Oppenheimer approximation [14].

Owing to the different charge states of NV^0 and NV^-, their nuclear coordinates and molecular orbitals differ [24, 25]. Thus, the reduced matrix elements demonstrate that both the orbital *g*-factor and spin-orbit parameter will differ between the two charge states due to the molecular orbital differences, and the spin-orbit parameter will additionally differ due to differences in the electrostatic potential V_{Ne}. This additional dependence of the spin-orbit parameter over the orbital *g*-factor is the likely reason why the parameter reduction differ when comparing NV^0 and NV^-.

Our observations do not immediately explain why fine structure has not been observed in EPR or PLE measurements of the NV^0 ground-state. Based on the spin-orbit parameter determined here and assuming the use of a 9.6 GHz X-band EPR spectrometer, the NV^0 ^2E EPR features are expected to be at $B=\pm(\pm f-2\lambda)/\mu_B g=\pm 0.16$T, ± 0.50T which are within the available field range of a typical X-band EPR spectrometer. Additionally, it has been shown that strong illumination with a green laser can photo-convert NV^- to NV^0. Thus, samples could be conveniently pumped to contain more NV^0 centers [12, 13]. Additionally, a tunable high-resolution laser should also be able to see these features in PLE.

We believe that there are three major reasons why the EPR signals of the ^2E were previously observed: (1) A reduction in angular momentum could also be influenced by fast averaging over the orbital states by a weak JT coupling to a bath of acoustic *E* modes. This is seen in the NV^- ^3E state at room temperatures [26, 27] as a removal of spin-orbit splittings. The remaining EPR signal would then be obscured by other spin-1/2 paramagnetic spins in the diamond sample, primarily the substitutional nitrogen or P1 center. (2) Another reason would be if there is a large-strain broadening of the resonances. For the limit of a strain distribution width (Γ) which is larger than spin-orbit splitting ($\Gamma\gg\lambda$), only a central spin-1/2 resonance remains. This will be obscured for the same reason mentioned above. (3) The final reason is that measurements have simply not been performed in the correct spectral range or the signal has been overlooked.

We have modeled the electron-phonon interactions and have found them to produce a negligible effect on the NV^0 spin resonances (see Supplementary information), ruling out the first reason. For explanation 3, it seems unlikely that the signal was overlooked, given targeted efforts to look for it [1], leaving explanation 2. We have modeled the second explanation (see Supplementary information) and we find that a wide strain distribution significantly reduces the contribution of the strained centers to the total EPR spectrum. We model this by introducing a strain shift to the spin resonances $\mathcal{E}$, resulting in the spin-resonances (neglecting $l=0.0186$) at $\mathcal{B}$ and $\mathcal{B}\pm\Delta$ where $\mathcal{B}=g\mu_B B_z$ and $\Delta=\sqrt{\lambda^2+\mathcal{E}^2}$. These spin resonances have the associated transition amplitudes $\cos^2\phi$ and $\sin^2\phi$, where $\phi=\tan(\mathcal{E}/\lambda)$. By constraining the oscillator strength to be conserved over the integrated spectral band, the intensity of the above resonances are $I_{\mathcal{B}}=\frac{\Gamma}{\Gamma+\lambda}$ and $I_{\mathcal{E}}=\frac{\lambda}{\Gamma+\lambda}$, where Γ is the width of the strain distribution, here assumed to be Lorentzian. In the limit that $\Gamma\gg\lambda$, then $I_{\mathcal{E}}\to 0$ and $I_{\mathcal{B}}\to 1$, resulting in spectra with a single resonance only at the free spin–1/2 resonance frequency, this behavior is demonstrated in Figure 4. The limit of $\Gamma\gg\lambda$ is reasonable, as the stress susceptibility and resulting width of the NV^0 orbital electronic states are both of order 100 s of GHz [5]. Note that the ensemble ZPL width in absorption of this particular sample (~50 GHz) is about 20 times narrower than the ensemble emission ZPL width presented by Davies [5] and Manson et al. [12].

The above arguments for EPR also apply to PLE measurements on a single NV^0. PLE should still observe some structure even in the presence of large strain. However, similar to EPR, in the large strain limit the PLE spectra will be modified to just show two transitions separated by a splitting $\mathcal{E}$, as such the fine-structure parameters cannot be extracted. This problem is general to measuring the PLE of any centre that has a Kramers doublet ground-state. For a Kramers doublet the degeneracy of the spin-levels will not be lifted by the strain and the eigenenergies will only add in quadrature with the applied strain splitting. This is not the same for NV^- ^3E as it is a not a Kramers doublet and PLE is routinely observed [20] (see figure 4 in the Supplementary information). Our fine structure parameters will put a lower bound on the expected PLE splitting, allowing for low-strain NV^0 single sites to be found via PLE.

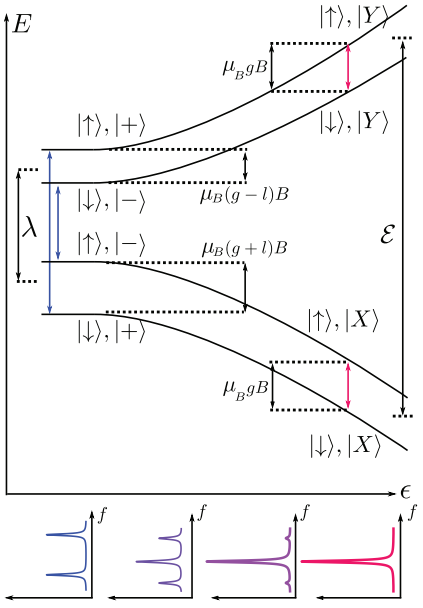

Figure 4: Behavior of ^2E spin-levels for increasing strain ($\mathcal{E}$) in a nonzero magnetic field.
In the high strain limit ($\mathcal{E} \gg \lambda$) the system is better represented by the $\{|X\rangle, |Y\rangle\}$ strain basis than the $\{|+\rangle, |-\rangle\}$ orbital basis. The colored arrows represent the observable electron paramagnetic resonance (EPR). For example, EPR spectra for increasing strain are shown at the bottom of the figure, with increasing strain from left to right. The spectra changes from exhibiting spin-orbit, orbital Zeeman, and spin Zeeman behavior to simple spin Zeeman behavior.

7 Conclusion

This work has determined the fine structure of the NV^0 electronic states using low temperature and high magnetic field MCD measurements and found agreement by using simple spin-Hamiltonians to describe the ground and excited states. The spin-orbit interaction in the NV^0 ground state $\lambda = 2.24 \pm 0.05$ GHz is found to be different to that of the NV^- excited state. This difference is attributed to the change in electrostatic potential associated to variations in the nuclear coordinates between the two charge states. There is significant quenching of the angular momentum with an orbital g-factor of $l = 0.0186 \pm 0.0005$. We have discussed why measurement of NV^0 ground-state fine structure has been elusive in previous EPR and PLE measurements and conclude that significant strain broadening of the ^2E resonances obscure the spin resonances.

8 Supplementary material

The Supplementary information can be found with the online version of the article.

Acknowledgments: We would like to acknowledge various funding sources for support during this work. In particular, NM would like to acknowledge the Australian Research Council through grants DP170103098. MD would like to acknowledge the Australian Research Council through grants DP170103098 and DE170100169. EK would like to acknowledge the Australian Research Council through grants DP110104565 and DP150103137.

References

[1] Felton S, Edmonds AM, Newton ME, Martineau PM, Fisher D, Twitchen DJ. Electron paramagnetic resonance studies of the neutral nitrogen vacancy in diamond. Phys Rev B 2008;77:081201.
[2] Haenens-Johansson UFSD, Edmonds AM, Green BL, et al. Optical properties of the neutral silicon split-vacancy center in diamond. Phys Rev B 2011;84:245208.
[3] Häußler S, Thiering G, Dietrich A, et al. Photoluminescence excitation spectroscopy of SiV^- and GeV^- color center in diamond. New J Phys 2017;19:063036.
[4] Jahnke KD, Sipahigil A, Binder JM, et al. Electron-phonon processes of the silicon-vacancy centre in diamond. New J Phys 2015;17:043011.
[5] Davies G. Dynamic Jahn-Teller distortions at trigonal optical centres in diamond. J Phys C: Solid State 1979;12:2551–6.
[6] Rogers LJ, Doherty MW, Barson MS, Onoda S, Ohshima T, Manson NB. Singlet levels of the NV- centre in diamond. New J Phys 2015;17:013048.
[7] Pfender M, Aslam N, Simon P, et al. Protecting a diamond quantum memory by charge state control. Nano Lett 2017;17:5931–7.
[8] Bourgeois E, Jarmola A, Gulka M, Hruby J, Budker D, Nesladek M. Photoelectric detection of electron spin resonance of nitrogen-vacancy centres in diamond. Nat Commun 2015;6:8577.
[9] Dhomkar S, Henshaw J, Jayakumar H, Meriles CA. Long-term data storage in diamond. Sci Adv 2016;2:1–6.
[10] Piepho SB, Schatz PN. Group theory in spectroscopy: with applications to magnetic circular dichroism. Hoboken, New Jersey, USA, John Wiley & Sons, 1983.
[11] Stephens PJ. Magnetic circular dichroism. Annu Phys 1974;25:201–32.
[12] Manson NB, Hedges M, Barson MSJ, et al. NV-N^+ pair centre in 1b diamond. New Phys 2018;20:113037.
[13] Manson NB, Harrison JP. Photo-ionization of the nitrogen-vacancy center in diamond. Diamond Related Mater 2005;14:1705–10.
[14] Doherty MW, Manson NB, Delaney P, Hollenberg LC. The negatively charged nitrogen-vacancy centre in diamond: the electronic solution. New J Phys 2011;13:025019.
[15] Krausz E. Selective and differential optical spectroscopies in photosynthesis. Photosynth Res 2013;116:411–26.
[16] Lax M. The Franck-Condon principle and its application to crystals. J Chem Phys 1952;20:1752–60.
[17] Reddy NRS, Manson NB, Krausz ER. Two-laser spectral hole burning in a colour centre in diamond. Luminescence 1987;38:46–7.

[18] Hanzawa H, Nishikori H, Nisida Y, et al. Zeeman effect on the zero-phonon line of the NV center in synthetic diamond. Phys B: Conden Matter 1993;184:137–40.
[19] Braukmann D, Glaser ER, Kennedy TA, Bayer M, Debus J. Circularly polarized zero-phonon transitions of vacancies in diamond at high magnetic fields. Phys Rev B 2018;97:195448.
[20] Batalov A, Jacques V, Kaiser F, et al. Low temperature studies of the excited-state structure of negatively charged nitrogen-vacancy color centers in diamond. Phys Rev Lett 2009;102:195506.
[21] Tamarat P, Manson NB, Harrison JP, et al. Spin-flip and spin-conserving optical transitions of the nitrogen-vacancy centre in diamond. New J Phys 2008;10:045004.
[22] Ham FS. Dynamical Jahn-Teller effect in paramagnetic resonance spectra: orbital reduction factors and partial quenching of spin-orbit interaction. Phys Rev 1965; 138:A1727–40.
[23] Ham FS. Effect of linear Jahn-Teller coupling on paramagnetic resonance in a ^2E state. Phys Rev 1968;166:307–21.
[24] Doherty MW, Manson N, Delaney BP, Jelezko F, Wrachtrup J, Hollenberg LCL. The nitrogen-vacancy colour centre in diamond. Phys Rep 2018;528:1–45.
[25] Gali A. Theory of the neutral nitrogen-vacancy center in diamond and its application to the realization of a qubit. Phys Rev B 2009;79:235210.
[26] Rogers LJ, McMurtrie RL, Sellars MJ, Mansonn NB. Time-averaging within the excited state of the nitrogen-vacancy centre in diamond. New J Phys 2009;11:063007.
[27] Plakhotnik T, Doherty MW, Manson NB. Electron-phonon processes of the nitrogen-vacancy center in diamond. Phys Rev B 2015;92:081203.

Supplementary Material: The online version of this article offers supplementary material (https://doi.org/10.1515/nanoph-2019-0142).